Robust graph-based denoising for cardiac acceleration signals

Salman Almuhammad Alali, Amar Kachenoura, Lotfi Senhadji, Alfredo Hernandez, Cindy Michel, Laurent Albera, Ahmad Karfoul

Highlights

Robust graph-based denoising for cardiac acceleration signals

Salman Almuhammad Alali, Amar Kachenoura, Lotfi Senhadji, Alfredo I. Hernandez, Cindy Michel, Laurent Albera, Ahmad Karfoul

- Efficient graph-based method for denoising cardiac ACC signals
- Pseudo-periodicity of cardiac cycles as a relevant feature for denoising ACC signals
- Targeting events of interest on well-tailored graph structures
- Denoising problem as constrained low-rank matrix inference one

Robust graph-based denoising for cardiac acceleration signals

Salman Almuhammad Alali[a], Amar Kachenoura[a], Lotfi Senhadji[a], Alfredo I. Hernandez[a], Cindy Michel[b], Laurent Albera[a,**] and Ahmad Karfoul[a,*]

[a]Univ Rennes, Inserm, LTSI - UMR 1099, Rennes, F-35000, France
[b]CardiaMetrics, La Tronche, Grenoble, France

ARTICLE INFO

Keywords:
Heart Failure
Denoising
Smoothness on graph
Low-rank estimation
Group sparsity

ABSTRACT

This paper proposes an efficient approach for denoising heart vibration signals captured by a 3D accelerometer in an implantable device located in the gastric fundus, aimed at improving heart failure monitoring. The approach leverages the inherent consistency (i.e. pseudo-periodicity) of heart vibration signals across cardiac cycles, reformulating the denoising problem as the inference of a low-rank matrix under the assumption of signal smoothness on graph structures associated with the target signals. Both the group sparsity and the total graph variation concepts are employed to describe the aforementioned assumptions. The effectiveness of this method, compared to standard denoising techniques, is confirmed by using real 3D accelerometer signals acquired from seven pigs with and without heart failure.

1. Introduction

Heart Failure (HF) poses a significant public health challenge, a concern that is exacerbated by aging populations and currently impacting around 64 million patients worldwide [1, 2]. The severity of HF is evidenced by frequent unplanned hospitalizations resulting from Acute Decompensated HF (ADHF). Hospitalizations are a common occurrence among HF patients and are associated with increased mortality, higher rates of readmission and economic burden [3]. These acute episodes have a bleak prognosis, with patients hospitalized twice facing a 40% risk of death within the following year. Longitudinal monitoring of cardiovascular biomarkers is adequate for a continuous patient follow-up and early detection of ADHF events, thereby providing tailored personalized therapy [4, 5, 6] and alleviating the economic burden. Recent advancements have shown the potential of implantable devices to fulfill the aforementioned requirements. Indeed, such a device enables continuous monitoring of cardiac function without the need of frequent supervision from clinicians or active patient involvement in data collection [7]. However, despite these technological advancements, there is still a real need to develop methods that can reliably collect high-quality longitudinal heart-related recordings [4].

For this purpose, our research group has recently proposed a novel implantable device designed for minimally invasive placement in the gastric fundus [4, 8]. This implantable device is equipped with a 3D accelerometer to capture heart ACCeleration (ACC) signals that reflect cardiomechanical activity, complemented by an ECG module for cardio-electrical activity acquisition. Numerous studies have highlighted the significance of leveraging ACC signals as a viable alternative to the PhonoCardioGram(PCG) ones, renowned for its relevance for monitoring heart conditions. More precisely, PCG signals are mainly characterized by two key components S1 and S2 sounds, occurring with each heartbeat, that are crucial for monitoring heart conditions [9, 10, 11, 12, 13]. The S1 sound marks the beginning of heart contraction through the closing of the atrioventricular valves, whereas the S2 sound, caused by the closure of the semilunar valves, indicates heart relaxation. In a previous work [4], a signal processing chain has been proposed to analyze the signals acquired by the above-mentioned implant, enabling the segmentation of the ACC signals and the identification of critical S1 and S2 cardiac events. The findings during pre-clinical experiments on pigs demonstrated the viability of long-term cardiovascular monitoring using such a gastric implant, for early medical intervention. However, the main remaining challenge involves the improvement of the signal-to-noise ratio (SNR), particularly in managing the inevitable complex noise generated by multiple sources associated with the gastric acquisition site. This complex noise, stemming from physiological activities like respiration and movements of internal organs, can mask the critical S1 and S2 events in the signals, posing difficulty in precisely diagnosing heart conditions [4]. Graph Signal Processing (GSP) has emerged recently as a promising framework for handling structured data [14] with efficacy being confirmed in various real-world applications. These include sensor networks [15], human brain [16], image and video processing [17, 18, 19, 20], as well as artificial intelligence and data science [21, 22, 23, 24].

In this paper, a GSP-based denoising approach is proposed to address the noise issue in the acquired 3D ACC signals using the recently proposed implantable device. Unlike conventional denoising techniques such as Principal Component Analysis (PCA) [25], Independent Component Analysis (ICA) Canonical Correlation Analysis (CCA) [26], the graph-based denoising approach delves deeper into the

⋆This work was supported in part by the ANR-DiGS project, in part by Brittany Region DeMuG project 2497 and in part by the PEPR Santé Numérique; Projet DIIP-HEART: ANR-22-PESN-0018.

*Corresponding author
**Co-last author
ahmad.karfoul@univ-rennes.fr (.A. Karfoul)
ORCID(s): 0000-0002-3977-9141 (.A. Karfoul)

structure of the signal under study. This structure, which is well qualified as irregular [15], is not conducive to the aforementioned standard denoising methods that are defined in the Euclidean space. The main idea of the proposed approach is to leverage the inherent consistency (i.e., pseudo-periodicity) of the events of interest, namely the S1 and S2 heart sounds, over cardiac cycles. This reframes the denoising problem as inferring a low-rank matrix while promoting the smoothness of the graph signal over an adequate structure. To address this problem, two distinct graphs corresponding to the S1 and S2 heart events are constructed based on their physiological characteristics and pseudo-periodicity across cardiac cycles. With these specific graphs defined as proposed in this study, S1 and S2 heart events can be represented as smooth signals over their respective graphs. It is noteworthy that the low-rank matrix approximation problem combined with the smoothness on graph has been explored in several studies [27, 28, 29, 30, 31]. However, the low-rank matrix inference problem is typically addressed by minimizing the nuclear norm, which often leads to computationally prohibitive optimization algorithms. To overcome this limitation, the mixed L21-norm is employed in the current study as it stands for a physiologically interpretable, low-cost, and more tractable alternative. In fact, recent research of our group has demonstrated that, beyond its cost-effectiveness and tractability, the mixed L21-norm is a better candidate than the nuclear norm for approximating the rank function, especially when the target matrix is full-column rank [32].

A comparative analysis to assess the performance of the proposed method relative to several well-known signal processing techniques. The evaluation encompasses classical matrix factorization approaches, including PCA [25], CCA [33], and ICA [34]; adaptive multiscale decomposition methods such as Empirical Mode Decomposition (EMD) [35], transform-based approaches like Wavelet analysis [36] and a Deep Learning (DL)-based method utilizing Convolutional Neural Networks (CNNs) [37] recently proposed by our group.

The main contributions in this study are:

- A graph-based denoising of ACC signals that lies on the intrinsic pseudo-periodicity of the events of interest (here S1 and S2 heart sounds) over cardiac cycles. Specifically, the denoising task is cast as the inference of a low-rank matrix subject to the smoothness of the events of interest on tailored graph structures that encode the aforementioned pseudo-periodicity property.
- Denoising performance that not only removes noise and isolated artifacts but also preserves the morphological characteristics of heart sounds.
- Significant SNR improvement for S1 and S2 heart sounds compared to well-established unsupervised and supervised denoising approaches.

The remainder of this paper is organized as follows: Section 2 outlines the notations and definitions used throughout this paper. Section 3 provides a detailed description of the dataset employed in the study. Section 4 presents the proposed methodology, including the observation model, graph construction process, and the optimization problem being addressed. Experimental results and the discussion of the findings are presented in Section 5. Finally, Section 6 provides the conclusion along with key highlights and potential directions for future work.

2. Notations and definitions

Throughout this paper, scalars are denoted by italic lowercase letters (e.g., a), vectors by bold lowercase letters (e.g., $\mathbf{a}$), and matrices by bold uppercase letters (e.g., $\mathbf{A}$). Sets are represented by blackboard bold type (e.g., $\mathbb{E}$), with $|\mathbb{E}|$ indicating the cardinal of the set $\mathbb{E}$. The n-th component of a vector $\mathbf{a}$, the (i,j)-th entry and the n-th column vector of a matrix $\mathbf{A}$ are denoted by a_n, $A_{i,j}$ and $\mathbf{a}_n$, respectively. The Frobenius norm of a matrix is denoted by $\|.\|_F$, Tr(.) is the matrix trace. The max(.) operator returns the largest component of its argument vector and $(.)^\top$ stands for the transposition operator. Besides, the operator $\odot$ denotes the Hadamard product (i.e., element-wise matrix product) and $\mathbf{I}_N$ is the identity matrix of size $N \times N$. The L2-norm and L21-norm are denoted respectively by $\|\cdot\|_2$ and $\|\cdot\|_{2,1}$, with

$$\|\mathbf{A}\|_{2,1} = \sum_i \sqrt{\sum_j |A_{i,j}|^2} = \mathrm{Tr}(\mathbf{A}^\top \mathbf{\Gamma} \mathbf{A}) \tag{1}$$

The entries of the diagonal matrix $\mathbf{\Gamma}$ are defined as

$$\Gamma_{i,i} = \frac{1}{\sqrt{\sum_{j=1}^{J} |A_{i,j}|^2}}$$

Definition 1: An undirected, unweighted graph $\mathcal{G}(\mathbb{V}, \mathbb{E}, \mathbf{A})$ is a collection of N nodes (vertices), defined in the set $\mathbb{V}$ of graph nodes ($N = |\mathbb{V}|$) that are interconnected by a set of edges gathered in $\mathbb{E}$. The interaction among the graph nodes is fully encoded in the symmetric adjacency matrix $\mathbf{A}(N \times N)$ defined as follows:

$$A_{i,j} = \begin{cases} 1, & \text{if nodes } i \text{ and } j \ (i \neq j) \text{ are connected,} \\ 0, & \text{otherwise.} \end{cases} \tag{2}$$

More precisely, each non-zero entry of $\mathbf{A}$ encodes a similarity between the associated pair of nodes. This similarity is possibly measured in terms of correlations, coherence, etc.
Definition 2: The graph Laplacian matrix $\mathbf{L}$ associated with $\mathcal{G}(\mathbb{V}, \mathbb{E}, \mathbf{A})$ is given by

$$\mathbf{L} = \mathbf{D} - \mathbf{A} \tag{3}$$

where $\mathbf{D} \in \mathbb{R}^{N \times N}$ denotes the degree matrix, which is a diagonal matrix, such that

$$D_{i,i} = \sum_{j=1}^{N} A_{i,j}$$

Definition 3: A graph signal is a function $f : \mathbb{V} \rightarrow \mathbb{R}$ that assigns a real number to each graph node. Therefore, the n-th component of the N-dimensional graph signal stands for the value of the graph signal at the n-th graph node (see Figure 1).

Definition 4: A smooth signal on a graph $\mathcal{G}(\mathbb{V}, \mathbb{E}, \mathbf{A})$ is a signal that exhibits a slow variation over the graph nodes. An example of a non-smooth and conversely a smooth signal on a graph established from five mechanical cardiac cycles are illustrated in Figure 1 (a) and Figure 1 (b), respectively. The smoothness of a graph signal $\mathbf{x}$ over $\mathcal{G}(\mathbb{V}, \mathbb{E}, \mathbf{A})$, or the total graph signal variation in a more general term, is quantified using the Laplacian quadratic form defined as follows [14]:

$$\Delta_{\mathbf{L}}(\mathbf{x}) = \sum_{i,j \in \mathbb{E}} A_{i,j}(x_i - x_j)^2 = \mathbf{x}^\top \mathbf{L}\mathbf{x} = \left\| \mathbf{L}^{1/2}\mathbf{x} \right\|_2^2 \quad (4)$$

where the summation is taken over all edges. According to equation (4), a low vs. high value of $\Delta_{\mathbf{L}}(\mathbf{x})$ corresponds to a smooth vs. non-smooth variation of the graph signal over the graph nodes (i.e., low vs. high frequency graph signal) [14], as shown on Figure 1b and Figure 1a, respectively.

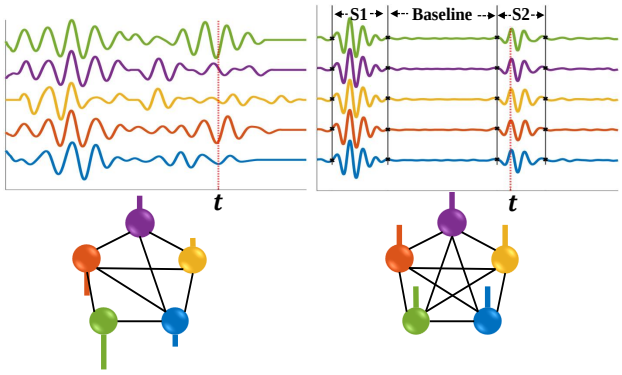

(a) High frequency graph signal (b) Low frequency graph signal

Figure 1: Smoothness of a signal on a graph comprising five interconnected nodes, each of which stands for a mechanical cardiac cycle. (a) case of a non-smooth (high frequency) graph signal; (b) case of a smooth (low frequency) graph signal.

3. Dataset

Synchronized ElectroCardioGrams (ECGs) and 3D ACC signals acquired via an implantable device located in the gastric fundus of seven pigs (four healthy and three with HF), are used in the current study. Two versions, V1 and V2 of this implant, shown in Figure 2, were used to collect the data: version V1 was used for healthy pigs while version V2 was used for those with HF. Both versions V1 and V2 recorded 3D ACC signals at a sampling rate of 4 kHz [4]. Observations were recorded during 30-seconds every hour over a period of 14 days. The noises and artefacts are mainly originating, on one hand, from the location of the implant in the gastric fundus and, on the other hand, from the implant

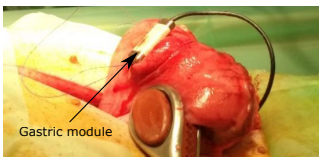

(a) Gastric module

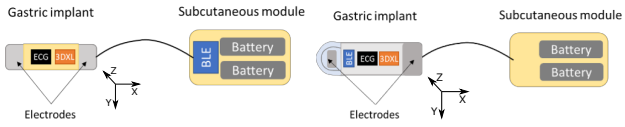

(b) Implant V1 (c) Implant V2

Figure 2: Implant prototypes used for acquiring the ECG and ACC data, (a) A module at the pig gastric site (b) Schematic representation of the implant V1, (c) Schematic representation of implant V2 [4].

itself. Location-induced noise encompasses gastric disturbances, movements of adjacent muscles, and various sounds from the pigs, including growls and digestive noises. Device-related noise involves data saturation issues, stemming from the implant's hourly transitions between sleep and active modes [4].

4. Methodology

4.1. Observation model

The mechanism of heart function involves quasi-repetitive electrical and mechanical actions that result in consistent patterns of electrical and mechanical activities throughout the ACC cardiac cycles. These activities can be monitored using various implantable cardiac devices, including the recently proposed gastric one [4]. As depicted in Figure 2, the gastric implant is equipped with an accelerometer and ECG modules that enable the recording of both the heart's mechanical and electrical activities. From now on and following [4], the term ACC signal will refer to the cardiac ACC signals which are acquired using the embedded 3D accelerometer. As pointed out previously, acquired ACC signals are tainted by various forms of noise and artefacts associated with the gastric site. The presence of such activities impedes the precise detection of critical heart events, specifically S1 and S2 sounds, and subsequently hinders the reliable monitoring of heart functions. To address this issue, the current study entails denoising each ACC axis separately through a graph-based formulation of the denoising problem. Here, the description of the proposed method focuses on a single ACC axis, keeping in mind that it can be similarly applied to all ACC axes. Let $\mathbf{Y} \in \mathbb{R}^{N \times T}$ denote the observation matrix, constructed by gathering N T-length cardiac cycles from the ACC signal under consideration. Here, T is defined as the duration of the longest cardiac cycle in the recording, and all shorter cycles are zero-padded to this length. Subsequently, the observation matrix is assumed to follow the linear model:

$$\mathbf{Y} = \mathbf{\Psi} + \mathbf{B}, \tag{5}$$

where $\mathbf{\Psi} \in \mathbb{R}^{N\times T}$ is a low-rank matrix comprising the clean cardiac cycles matrix including S1 and S2 events, and $\mathbf{B} \in \mathbb{R}^{N\times T}$ accounts for an additive noise matrix. As the S1 and S2 cardiac events show intrinsic consistency throughout the cardiac cycles, each column vector of $\mathbf{\Psi}$ wich is associated with a given time sample, can be figured out as a smooth graph signal. More precisely, such a column vector exhibits low variation over two graph structures, $\mathcal{G}_{\text{S1}}(\mathbb{V}_{\text{S1}}, \mathbb{E}_{\text{S1}}, \mathbf{A}_{\text{S1}})$ and $\mathcal{G}_{\text{S2}}(\mathbb{V}_{\text{S2}}, \mathbb{E}_{\text{S2}}, \mathbf{A}_{\text{S2}})$ associated with the cardiac events of interest (S1 and S2) and constructed from the segmented cardiac ACC cycles (see more details in Section 4.2). Besides, it is worth noting that for a clean ACC signal, the columns of $\mathbf{\Psi}$ that are related to baseline segments (i.e., segments between S1 and S2 events as shown in Figure 1) are assumed to be all-zero vectors, as these segments are devoid from any activity of interest. Thus, with regard to the consistency among cardiac cycles and the presence of all-zero vectors that the matrix $\mathbf{\Psi}$ is enjoying, the low-rank assumption on $\mathbf{\Psi}$ holds valid.

4.2. Graph Construction

Let $\mathcal{G}_\theta(\mathbb{V}_\theta, \mathbb{E}_\theta, \mathbf{A}_\theta), \theta \in \{\text{S1}, \text{S2}\}$ be the graph associated to the heart sound θ where $\mathcal{G}_\theta$ encodes the intrinsic consistency of this event overall the available segmented ACC cardiac cycles. In this study, the n-th node in $\mathcal{G}_\theta$ is associated with the time segment of the n-th cardiac cycle where the event θ occurs. Notably, unlike the waveform consistency of S1 and S2 heart sounds throughout the ACC cardiac cycles, these signals exhibit slight variations in their respective start and end times across cycles due to Heart Rate Variability (HRV) [38]. Thus, two nodes in $\mathcal{G}_\theta$ are assumed to be connected if their associated consistency, measured here in terms of the cross-correlation, exhibits a value that is higher than 0.6 (more details about the choice and the relevance of this value is given in supplementary materials-Section I). More precisely, a cross-correlation matrix, denoted here by $\mathbf{C} \in \mathbb{R}^{N\times N}$ whose (i, j)-th entry, $C_{i,j}$, refers to the maximum normalized cross-correlation coefficient among a set of normalized cross-correlation coefficients computed at different time-lags (i.e., considering HRV), is computed. The normalized cross-correlation coefficient between the i-th and j-th, $1 \leq i \neq j \leq N$, graph nodes, at a given time-lag τ, is given by:

$$C_{i,j}(\tau) = \frac{\sum_{t=1}^{T-\tau} Y_{i,t} Y_{j,t+\tau}}{\sqrt{\sum_{t=1}^{T} Y_{i,t}^2}\sqrt{\sum_{t=1}^{T-\tau} Y_{j,t+\tau}^2}}, \tag{6}$$

Once the matrix $\mathbf{C}$ is computed, the derivation of the associated adjacency matrix, $\mathbf{A}_\theta$, and subsequently the graph Laplacian one, $\mathbf{L}_\theta$, is straightforward according to equation (2), for a threshold value of 0.6 as pointed out above, and Definition 2, respectively. More specifically, the S1 event occurs within the first half of the cardiac cycle, corresponding to the systole phase, while the S2 event takes place during the diastole phase in the latter half of the cycle [39]. Consequently, the first graph, $\mathcal{G}_{\text{S1}}$, was created based on the cross-correlation coefficients between the first half of the cycles, while the second graph, $\mathcal{G}_{\text{S2}}$, was built using the cross-correlation coefficients between the last 60% of heart cycles, suggesting a 10% overlap to handle HRV.

4.3. Optimization problem

Under the intrinsic low-rank property of the latent matrix $\mathbf{\Psi}$ together with the fact that each of its column vector is a smooth graph signal on $\mathcal{G}_{\text{S1}}$ and $\mathcal{G}_{\text{S2}}$,denoising the observed cardiac ACC signals can be summed up to minimizing, with respect to $\mathbf{\Psi}$, the following cost function:

$$\begin{aligned}\underset{\mathbf{\Psi}}{\text{Minimize}} \quad & \|\mathbf{Y} - \mathbf{\Psi}\|_F^2 + \lambda_1 \|\mathbf{\Psi}\|_{2,1} + \lambda_2 \left\|\mathbf{L}_{\text{S1}}^{1/2}\mathbf{\Psi}\right\|_F^2 \\ & + \lambda_3 \left\|\mathbf{L}_{\text{S2}}^{1/2}\mathbf{\Psi}\right\|_F^2\end{aligned} \tag{7}$$

where the mixed L21-norm encodes the low-rank property of $\mathbf{\Psi}$ as recently shown in [32], and λ_1, λ_2 and λ_3 stand for the penalty parameters. It can be clearly stated that the above optimization problem is convex but non-differentiable due to the mixed L21-norm. Typically, this problem can be solved within the proximal optimization framework by computing the proximal operator associated with the mixed L21-norm, which is a complex and tedious task. To address this limitation, the optimization problem can be reformulated as an iterative process alternating **i)** the minimization with respect to $\mathbf{\Psi}$ of a convex and cost differentiable function given by:

$$\begin{aligned}g(\mathbf{\Psi}) = \ & \|\mathbf{Y} - \mathbf{\Psi}\|_F^2 + \lambda_1 \operatorname{Tr}(\mathbf{\Psi}^\top \mathbf{\Gamma} \mathbf{\Psi}) + \lambda_2 \left\|\mathbf{L}_{\text{S1}}^{1/2}\mathbf{\Psi}\right\|_F^2 \\ & + \lambda_3 \left\|\mathbf{L}_{\text{S2}}^{1/2}\mathbf{\Psi}\right\|_F^2\end{aligned} \tag{8}$$

where $\mathbf{\Gamma}$ is a constant diagonal matrix assumed, at this stage, to be independent from $\mathbf{\Psi}$; and **ii)** the update of $\mathbf{\Gamma}$ recalling then, as pointed out in Section 2, its mathematical dependence on $\mathbf{\Psi}$. In fact, the full independence being first assumed between $\mathbf{\Psi}$ and $\mathbf{\Gamma}$ enables the estimation of $\mathbf{\Psi}$ in a closed form solution by computing the stationary point of g in (8) with respect to $\mathbf{\Psi}$. This leads to estimate $\mathbf{\Psi}$ as follows:

$$\mathbf{\Psi} = \left(\mathbf{I}_N + \lambda_1 \mathbf{\Gamma} + \lambda_2 \mathbf{L}_{\text{S1}} + \lambda_3 \mathbf{L}_{\text{S2}}\right)^{-1} \mathbf{Y} \tag{9}$$

Next, the diagonal matrix $\mathbf{\Gamma}$ is derived from the last estimate of $\mathbf{\Psi}$ by recalling that these two matrices are linked as follows (see Section 2):

$$\Gamma_{i,i} = \frac{1}{\sqrt{\sum_{j=1}^{J} |\Psi_{i,j}|^2}} \tag{10}$$

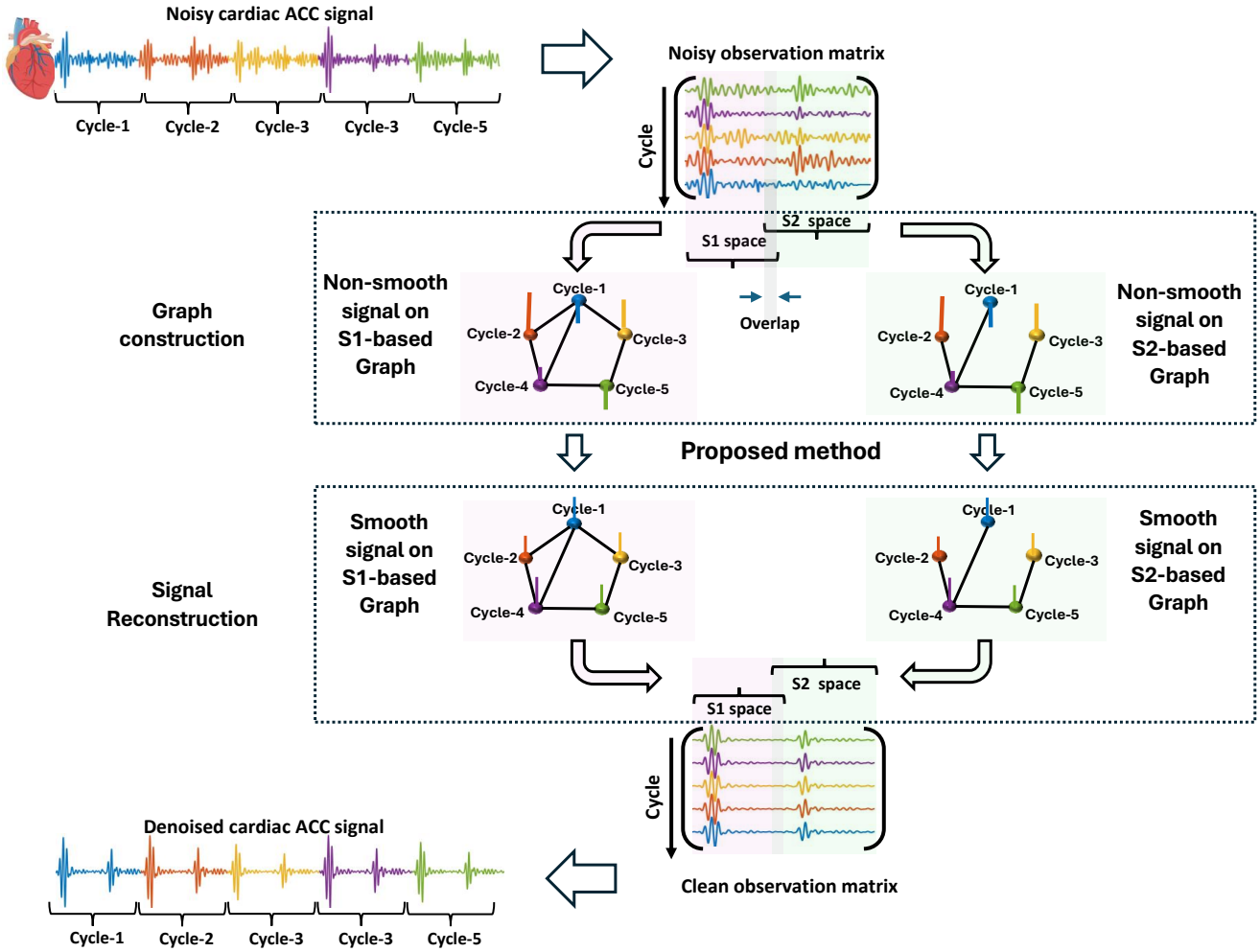

Figure 3: Diagram of proposed graph-based denoising method.

Then, following an expectation-maximization like scheme, the optimization procedure operates on an alternative estimation of both $\mathbf{\Psi}$ and its associated diagonal matrix $\mathbf{\Gamma}$.
At each iteration of the proposed approach, the matrices $\mathbf{\Psi}$ and $\mathbf{\Gamma}$ are computed alternately, with each matrix being updated while the other is fixed to its last estimate. This process is repeated until the relative error in the estimation of $\mathbf{\Psi}$ between two successive iterations exhibits a value less than a predefined threshold, or until a maximum number of iterations is reached. Note that solving the optimization problem as proposed in this paper implicitly boils down to the well-known block coordinate optimization problem, but with the involved variables being highly dependent rather than independent. However, despite the dependencies between the involved matrices (i.e. $\mathbf{\Psi}$ and $\mathbf{\Gamma}$), the block-coordinate approach still demonstrates convergence, as recently shown in [40, 41]. A visual illustration of the proposed graph-based denoising methods is given in Figure 3.

4.4. Sensitivity analysis

As the optimization problem at hand requires the three penalty parameters, λ_1, λ_2, and λ_3, to be wisely fixed, a sensitivity analysis to identify the influence of each parameter is mandatory prior to the selection of their adequate respective values. To this end, a sensitivity analysis using the well-known Morris method is performed [42]. More specifically, the parameters were varied in the range $[0.01, 50]$ to assess their impact on denoising performance with respect to both $\mathrm{SNR}_{\mathrm{S1}}$ and $\mathrm{SNR}_{\mathrm{S2}}$. Morris' analysis reveals, as shown in Figure 4, that among the three penalty parameters, λ_2 consistently exerts the most significant influence. It produces both the highest average elementary effect and the greatest variability, indicating a strong impact on denoising performance of the proposed method and notable sensitivity to interactions with the other parameters. In contrast, λ_3 demonstrates a moderate mean effect and moderate variability, suggesting that while tuning it can yield additional improvements, these gains are relatively limited and more stable. Finally, λ_1 shows minimal and consistent influence, as its mean effect remains close to zero.

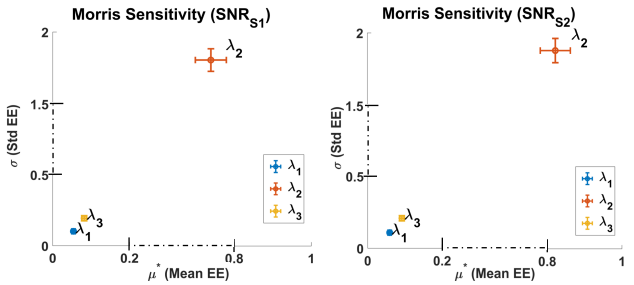

(a) SNR$_{S1}$

Figure 4: Morris sensitivity analysis shows Mean and standard deviation of Elementary Effect (EE).

5. Results and discussion

In this section, the performance of the proposed graph-based approach for denoising 3D ACC signals acquired from gastric implant, of 4 healthy pigs and 3 pigs with HF, is evaluated and compared to established denoising techniques such as PCA [25], CCA [33], EFICA [34], EMD [35] and Wavelet [36], as well as the DL-based technique recently proposed in [37]. The PCA, CCA, and EFICA methods were applied to each 3D ACC record representing a spatio-temporal observation matrix of size (number of axes × record length). EMD, Wavelet, and DL-based methods were applied to each ACC axis separately. Regarding the proposed graph-based approach, it was also applied to each ACC axis separately, as described in Section 4. However, before assessing the effectiveness of the proposed method, we introduce hereafter the strategy being adopted to fix the suitable triplet of the regularization parameters, $(\lambda_1, \lambda_2, \lambda_3)$.

5.1. Selection of regularization parameters

Based on the Morris sensitivity analysis discussed in Section 4.4, λ_1 has the lower influence on the proposed method performance, thus, we fix $\lambda_1 = 1$ and focus our optimization efforts on λ_2 and λ_3 which have the highest effect on the performance of the proposed method. With this latter choice of λ_1 value, a grid search over several candidate values of λ_2 and λ_3 is performed to find the best value of the triplet $(1, \lambda_2, \lambda_3)$ in terms of SNR improvement. According to Figure 5, a subset of $(1, \lambda_1, \lambda_2)$ triplets yields the highest SNR improvements for the S1 and S2 events across the ACC axes. Consequently, for all the results presented below, the triplet $(1, 2, 10)$ was selected in accordance with the proposed method (See pink square highlighted in Figure 5).

Note that for a fair comparison, similar to our proposed method, each benchmark approach also requires tuning of some parameters to achieve its best SNR improvement. More precisely, for PCA, all combinations of the three principal components (individual components, pairs, and the full set) were evaluated, and the combination that yielded the highest SNR for S1 and S2 events in each recording was selected. Similarly, for CCA and EFICA, we tested all possible combinations of source components derived from the 3D ACC signal. For EMD, several levels of Intrinsic Mode Functions (IMFs) were tested, with the best performance achieved using the first three IMFs from an 8-level decomposition. Regarding the Wavelet approach, we evaluated multiple Wavelet families and decomposition levels. The biorthogonal 3.9 Wavelets at five decomposition levels provide optimal results. As far as DL-based method is concerned, the CNN denoising filter was selected using a greedy search strategy as described in [37], and the filter that resulted in the best SNR improvement was retained.

5.2. Evaluation of denoising performance

The addressed approaches were assessed based on their respective improvements in the SNR of S1 and S2 segments. To this end, the terms $\mathrm{SNR}^{\theta}_{\mathrm{denoised}}$ and $\mathrm{SNR}^{\theta}_{\mathrm{noisy}}$, will refer to the SNR value of the segment $\theta \in \{\mathrm{S1,S2}\}$ after and before applying the denoising step, respectively. The values of $\mathrm{SNR}^{\theta}_{\mathrm{noisy}}$ were computed using the pipeline recently introduced by our group [4]. This pipeline involves calculating a coherent mean cardiac cycle from the input data (i.e., either $\mathbf{Y}$ or $\mathbf{\Psi}$) and segmenting it into S1 and S2 waves. These segments are then projected back, for a comprehensive segmentation, onto the entire heart cycles of the cardiac record under study. Note that the same pipeline was also used to calculate the $\mathrm{SNR}^{\theta}_{\mathrm{denoised}}$. An example of a segmented heart cycle is illustrated in Figure 6, highlighting the segments corresponding to the S1 and S2 heart sounds, as well as a noise/baseline activity segment. In the sequel, the $T_{\mathbf{v}}$-dimensional vector $\mathbf{v}$, with $T_{\mathbf{v}}$ being its time period will refer to the noise/baseline activity.

Then, the SNR of the event θ at the n-th, $n \in \{1, \cdots, N\}$, segmented ACC cardiac cycle is computed as suggested in [4, 43]:

$$\mathrm{SNR}^{\theta}_{\beta,n} = 10 \times \log_{10}\left(\frac{\max\left(\left(\mathbf{z}^{\theta}_{\beta,n}\right)^{\odot 2}\right)}{\frac{1}{T_{\mathbf{v}}}\sum_{i=1}^{T_{\mathbf{v}}}\left|\mathbf{v}_{\beta,n}[i]\right|^2}\right) \tag{11}$$

with $\beta \in \{\text{noisy, denoised}\}$ and where $\left(\mathbf{z}^{\theta}_{\beta,n}\right)^{\odot 2} = \mathbf{z}^{\theta}_{\beta,n} \odot \mathbf{z}^{\theta}_{\beta,n}$ with $\mathbf{z}$ being a T_{θ}-dimensional vector gathering the time samples constituting the event θ. Finally, the SNR enhancement index of the heart sound θ, denoted here by ξ^{θ}, is computed as follows:

$$\xi^{\theta} = \frac{\mathrm{SNR}^{\theta}_{\mathrm{denoised}} - \mathrm{SNR}^{\theta}_{\mathrm{noisy}}}{\left|\mathrm{SNR}^{\theta}_{\mathrm{noisy}}\right|} \times 100 \tag{12}$$

where $\mathrm{SNR}^{\theta}_{\beta} = \frac{1}{N}\sum_{n=1}^{N}\mathrm{SNR}^{\theta}_{\beta,n}$. λ_1, λ_2 and λ_3 are the penalty parameters of equation (9), their respective values (1, 2 and 10) are determined as discussed in Section 5.1.

Table 1 shows the mean and the standard deviation of the computed $\mathrm{SNR}^{\theta}_{\beta}$ over the N heart cycles for the three ACC axes X, Y, and Z. The proposed method demonstrates superior performance in denoising both S1 and S2 events when

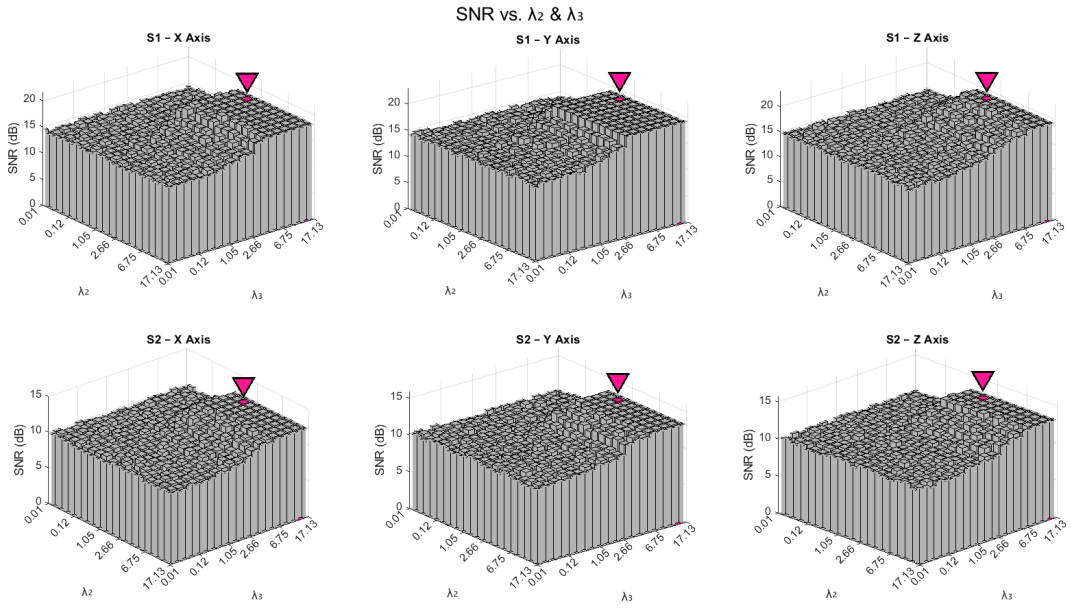

Figure 5: 3D bar-plot surfaces of SNR (dB) for signals S1 (top row) and S2 (bottom row) along the X, Y, and Z axes, as a function of regularization parameters λ_3 and λ_3 sampled logarithmically from 0.01 to 20. The bright pink bar and downward triangle at ($\lambda_2 = 2$, $\lambda_3 = 10$) highlight the operating point selected in our experiments.

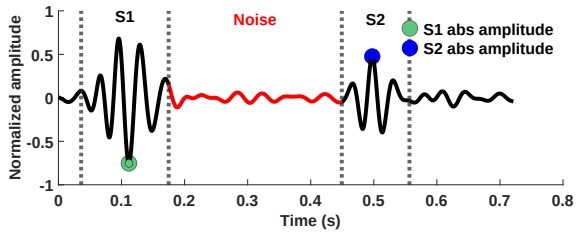

Figure 6: Segmented ACC heart cycle comprising both S1 and S2 heart events with a noise/baseline segment (in red).

compared to PCA, CCA, EFICA, EMD, Wavelet, and CNN. For instance, in the case of the X axis, the noisy ACC has a mean SNR of 14.3(9.9) dB for S1(S2) and the mean SNR values provided by PCA, CCA, EFICA, EMD, Wavelet, and CNN are 14.7(10.0) dB, 15.8(11.4) dB, 15.6(10.9) dB, 14.3(10.0), 14.4(10.1), and 16.9(11.7) respectively. This corresponds to respective SNR enhancement ratios of 3.4%(2.4%), 10.5%(14.6%), 9.2%(9.7%), 0.0%(1.4%), 0.6%(2.4%) and 18.2%(18.2%). In contrast, the proposed method achieves significantly higher mean SNR values of 18.2 dB for S1 and 12.4 dB for S2, indicating a higher enhancement in the SNR, even for the more challenging S2 wave due to its lower initial SNR value. In fact, the proposed method ends up with a higher SNR improvement of 27.5% for S1 and 24.8% for S2. A similar superior performance of the proposed method is also obtained for the Y and Z axes, shown in Table 1. These SNR improvements are further confirmed from a statistical perspective through a one-tailed t-test conducted on the set of $\text{SNR}_{\beta}^{\theta}$ values (obtained from all denoised ACC cycles) between the proposed approach and each of the considered standard methods, namely PCA, CCA, EFICA, EMD, Wavelet, and CNN. The p-values are $\leq 10^{-3}$ for denoising S1 and S2, whatever the compared classical method and the analyzed axes, demonstrating the significance superiority of the proposed method.

To complete our performance analysis study, a visual inspection of the performance of each denoising method is provided in Figure 8. This figure shows an example of denoising a set of ACC heart cycles extracted from a 29-second recording of axis Y of a gastric implantable device using PCA, CCA, EFICA, EMD, Wavelet, CNN, and the proposed method. Clearly, we can observe that the proposed approach promotes intrinsic consistency among different ACC cardiac cycles, with S1 and S2 heart sounds being properly denoised compared to the other standard denoising approaches. In addition, the proposed methodology demonstrates enhanced efficacy in accurately denoising the baseline segment situated between the S1 and S2 heart sounds, thereby yielding superior delineation of these cardiac events. Note that, similar denoising behavior is observed for the other two ACC axes (X and Z), whatever the used denoising method, as shown in supplementary material-Section II.

5.3. Impact of segmentation misalignment

As pointed out previously, the key idea of graph-based denoising method is to exploit the intrinsic pseudo-periodicity of the events of interest (here S1 and S2 heart sounds) over cardiac cycles. Indeed, the smoothness on graph assumption of the events of interest requires the alignment of ACC cycles. However, misalignment can be encountered in

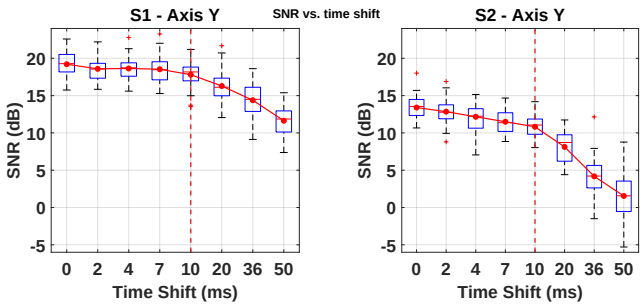

Figure 7: SNR degradation with time shift for S1 and S2 events across Y-axis.

practice due to the noise and heart variability. To assess the robustness of our approach in the presence of segmentation errors, we performed an analysis by intentionally introducing controlled misalignments at the boundaries of cardiac cycles. More precisely, we introduced random time shifts at the beginning of each cycle within the range of $[\pm 1, \pm 50]$ milliseconds to emulate realistic segmentation inaccuracies, such as those caused by R-peak detection variability or heart rate fluctuations. Figure 7 illustrates the SNR variation as a function of the introduced time shift for the Y axis. It can be noticed from the latter figure that the SNR improvement achieved by the proposed denoising approach for both S1 and S2 heart sounds demonstrates that the proposed method remains robust to time shifts up to approximately ± 10 ms. This demonstrates the robustness of the graph-based method with respect to the heart rate variability and the segmentation errors. Similar performance is obtained for the other ACC axes (X and Z) and provided as supplementary material-Section III.

5.4. On the limitation of the proposed approach

As claimed before, the proposed denoising approach is initially tailored to denoise heart sound waves (i.e., S1 and S2) captured through 3D-ACC signals in a very noisy environment. To this end, the pseudo-periodicity inherent to these events is exploited and encoded in a graph total variation constraint. In practice, this pseudo-periodicity assumption holds valid in several cardiac pathologies, such as chronic HF and right bundle branch block. In these cases, our proposed denoising methodology is well adapted. However, the same property (i.e., pseudo-periodicity of the target events) that makes the proposed method effective reduces its ability to preserve isolated or non-periodic events, which might be related to some pathologies. Indeed, these kinds of isolated patterns will be vanished on the expense of high denoising quality. This is because they do not fulfill the smoothness on graph constraint and consequently will be recognized as artifacts. To preserve these isolated patterns, for diagnostic perspectives, one can think about retuning the regularization parameters, but this would be at the expense of the denoising effectiveness.

5.5. Numerical complexity

The numerical complexity of the proposed method and the other considered ones is expressed in terms of numerical flops. Note that since there are more multiplications than additions, a numerical flop is accounted for only by the number of multiplications and additions required for each operation. For a detailed description of the computation of the numerical complexity of the proposed method, please refer to the supplementary material-Section IV. The numerical complexity of the proposed graph-based method is $\left(N^2 T \log T + k\left(N^3 + N^2 T\right)\right)$, where N is the number of variables, T the length of each signal, and k the number of components or iterations. Compared to the six considered methods (see Table IV, supplementary materials-Section IV), the graph-based method presents a numerical complexity comparable to PCA, CCA and ICA, and EFICA. EMD and Wavelet exhibit the lowest numerical complexity, while the CNN one is clearly of computational burden. To sum up and regarding the obtained denoising results, the proposed graph-based method provides the best complexity-denoising performance tradeoff.

6. Conclusion

In this paper, we proposed an efficient denoising approach for heart sounds captured by a 3D accelerometer embedded in an implantable device located in the gastric fundus. This approach leverages the intrinsic consistency of heart sounds across different cardiac cycles. The denoising problem was reformulated as the inference of a low-rank matrix under the constraints of a smooth signal on graph structures specifically tailored to the heart sounds of interest. The group-sparsity technique expressed by the L21-norm was used in this paper for the estimation of the low-rank matrix leading to a more tractable optimization problem. The combination of graph total variation and group sparsity techniques has proven effective in addressing the denoising problem, outperforming standard denoising methods. This efficacy was validated using real data acquired from seven pigs. Future work will focus on evaluating the proposed approach on a broader animal real-world dataset and also on investigating the automatic choice of the regularization parameters.

ETHICS STATEMENT

The animal study protocol was reviewed and approved by an ethics committee in compliance with the French Ministry of Research guidelines.

References

[1] B. Shahim, C. J. Kapelios, G. Savarese, L. H. Lund, Global public health burden of heart failure: an updated review, Cardiac Failure Review 9 (2023).

[2] G. Savarese, P. M. Becher, L. H. Lund, P. Seferovic, G. M. Rosano, A. J. Coats, Global burden of heart failure: a comprehensive and updated review of epidemiology, Cardiovascular research 118 (2022) 3272–3287.

Table 1
For each ACC axes, X, Y, and Z, the mean ± standard deviation of the estimated mean $SNR^{\theta}_{\beta}, \theta \in \{S1, S2\}, \beta \in \{noisy, denoised\}$, was computed over N cardiac cycles per recordings, for both S1 and S2 heart events.

Denoising	ACC S1			ACC S2		
Method	X	Y	Z	X	Y	Z
Non	14.3±6.2	14.8±6.1	14.8±6.1	9.9±6.1	10.3±6.4	10.1±6.0
PCA	14.7±6.3	15.2±6.1	15.0±6.3	10.0±6.0	10.6±6.2	10.3±6.1
CCA	15.8±5.8	15.7±5.7	15.6±5.9	11.4±6.0	11.3±6.1	11.1±6.1
EFICA	15.6±5.9	15.6±6.0	15.6±6.0	10.9±6.1	11.0±6.2	10.9±6.2
EMD	14.3±5.8	14.8±5.7	14.8±5.9	10.0±6.0	10.4±6.1	10.1±6.1
Wavelet	14.4±5.7	14.9±5.6	14.9±5.7	10.1±5.8	10.5±6.1	10.3±5.8
CNN	16.9±7.0	17.3±6.5	17.0±7.2	11.7±6.3	12.1±6.8	12.1±6.4
Proposed	**18.2±6.3**	**19.2±6.1**	**19.3±6.2**	**12.4±6.7**	**13.3±6.9**	**13.2±6.5**

Table 2
SNR improvement ratio, $\xi^{\theta}, \theta \in \{S1, S2\}$ of both S1 and S2 heart events overall the cardiac cycles

Denoising	ACC S1			ACC S2		
Method	X	Y	Z	X	Y	Z
PCA	3.4%	2.6%	1.0%	2.4%	2.9%	1.6%
CCA	10.5%	6.1%	5.6%	14.6%	10.1%	10.2%
EFICA	9.2%	5.8%	5.2%	9.7%	7.0%	7.6%
EMD	0.0%	0.6%	0.2%	1.4%	1.5%	0.7%
Wavelet	0.6%	0.6%	0.6%	2.4%	2.0%	2.1%
CNN	18.2%	17.3%	15.2%	18.2%	17.6%	20.0%
Proposed	**27.5%**	**29.5%**	**30.1%**	**24.8%**	**29.5%**	**30.4%**

[3] B. Bozkurt, G. Savarese, S. Adamsson Eryd, J. Bodegård, J. G. Cleland, C. Khordoc, T. Kishi, M. Thuresson, O. Vardeny, R. Zhang, et al., Mortality, outcomes, costs, and use of medicines following a first heart failure hospitalization: Evolution hf, Heart Failure 11 (2023) 1320–1332.

[4] H. Areiza-Laverde, C. Dopierala, L. Senhadji, F. Boucher, P. Y. Gumery, A. Hernández, Analysis of cardiac vibration signals acquired from a novel implant placed on the gastric fundus, Frontiers in Physiology 12 (2021) 748367.

[5] J. G. Cleland, J.-C. Daubert, E. Erdmann, N. Freemantle, D. Gras, L. Kappenberger, L. Tavazzi, Longer-term effects of cardiac resynchronization therapy on mortality in heart failure [the cardiac resynchronization-heart failure (care-hf) trial extension phase], European heart journal 27 (2006) 1928–1932.

[6] A. S. Desai, A. Bhimaraj, R. Bharmi, R. Jermyn, K. Bhatt, D. Shavelle, M. M. Redfield, R. Hull, J. Pelzel, K. Davis, et al., Ambulatory hemodynamic monitoring reduces heart failure hospitalizations in "real-world" clinical practice, Journal of the American College of Cardiology 69 (2017) 2357–2365.

[7] M. M. H. Shandhi, B. Semiz, S. Hersek, N. Goller, F. Ayazi, O. T. Inan, Performance analysis of gyroscope and accelerometer sensors for seismocardiography-based wearable pre-ejection period estimation, IEEE journal of biomedical and health informatics 23 (2019) 2365–2374.

[8] C. Dopierala, P.-Y. Gumérya, M.-R. Frikhaa, J.-J. Thiébaulta, P. Cinquina, F. Bouchera, Digital implantable gastric stethoscope for the detection of early signs of acute cardiac decompensation in patients with chronic heart failure, Actes LAtelier Ia Sante (2019).

[9] A. I. Hernández, F. Ziglio, A. Amblard, L. Senhadji, C. Leclercq, Analysis of endocardial acceleration during intraoperative optimization of cardiac resynchronization therapy, in: 2013 35th Annual International Conference of the IEEE Engineering in Medicine and Biology Society (EMBC), IEEE, 2013, pp. 7000–7003.

[10] C. Gallet, V. Le Rolle, J.-L. Bonnet, C. Henry, A. Hagège, P. Mabo, G. Carrault, A. I. Hernández, Analysis of endocardial micro-accelerometry during valsalva maneuvers, in: 2016 Computing in Cardiology Conference (CinC), IEEE, 2016, pp. 21–24.

[11] G. Plicchi, E. Marcelli, M. Parlapiano, T. Bombardini, Pea i and pea ii based implantable haemodynamic monitor: pre clinical studies in sheep, Europace 4 (2002) 49–54.

[12] P. Bordachar, S. Garrigue, P. Ritter, S. Ploux, L. Labrousse, C. Casset, M. Haissaguerre, P. Dos Santos, Contributions of a hemodynamic sensor embedded in an atrial lead in a porcine model, Journal of Cardiovascular Electrophysiology 22 (2011) 579–583.

[13] P. Bordachar, L. Labrousse, S. Ploux, J.-B. THAMBO, S. Lafitte, P. Reant, P. Jais, M. Haissaguerre, J. Clementy, P. D. SANTOS, Validation of a new noninvasive device for the monitoring of peak endocardial acceleration in pigs: implications for optimization of pacing site and configuration, Journal of cardiovascular electrophysiology 19 (2008) 725–729.

[14] D. I. Shuman, S. K. Narang, P. Frossard, A. Ortega, P. Vandergheynst, The emerging field of signal processing on graphs: Extending high-dimensional data analysis to networks and other irregular domains, IEEE signal processing magazine 30 (2013) 83–98.

[15] W. Huang, L. Goldsberry, N. F. Wymbs, S. T. Grafton, D. S. Bassett, A. Ribeiro, Graph frequency analysis of brain signals, IEEE Journal of Selected Topics in Signal Processing 10 (2016) 1189–1203.

[16] A. Karfoul, A. Kachenoura, L. Albera, A unified approach for inverse problem in EEG and brain connectivity with application to epilepsy. a proof of concept study, in: 2023 31st European Signal Processing Conference (EUSIPCO), IEEE, 2023, pp. 1713–1717.

[17] D. Thanou, P. A. Chou, P. Frossard, Graph-based compression of dynamic 3d point cloud sequences, IEEE Transactions on Image Processing 25 (2016) 1765–1778.

[18] C. Couprie, L. Grady, L. Najman, J.-C. Pesquet, H. Talbot, Dual constrained tv-based regularization on graphs, SIAM Journal on Imaging Sciences 6 (2013) 1246–1273.

[19] S. Chen, D. Tian, C. Feng, A. Vetro, J. Kovačević, Fast resampling of three-dimensional point clouds via graphs, IEEE Transactions on Signal Processing 66 (2017) 666–681.

[20] Y.-L. Qiao, Y. Zhao, C.-Y. Song, K.-G. Zhang, X.-Z. Xiang, Graph wavelet transform for image texture classification, IET Image Processing 15 (2021) 2372–2383.

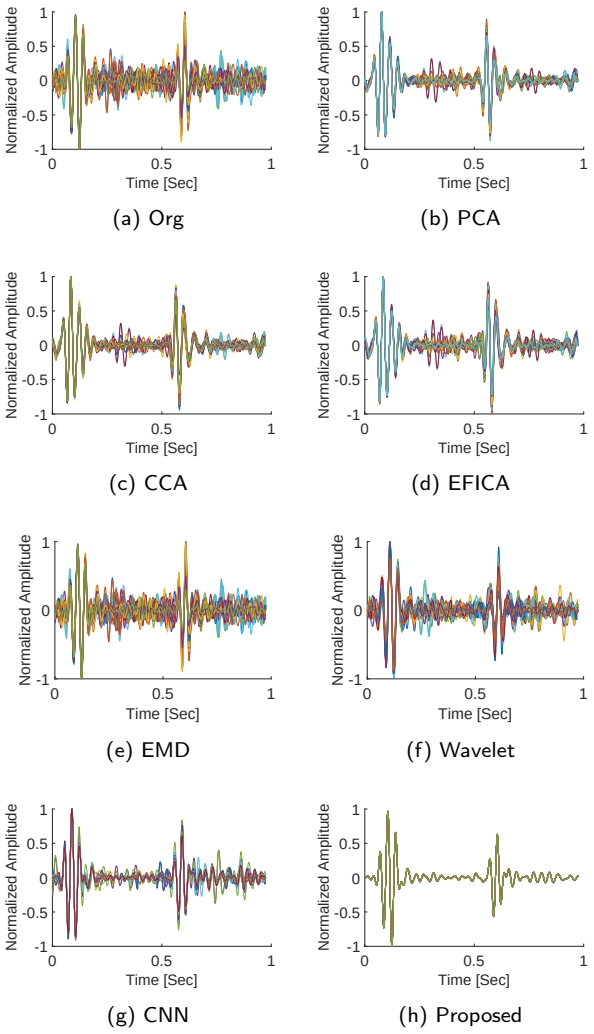

Figure 8: Denoising a set of ACC heart cycles extracted from a 29-second recording of a single accelerometer Y-axis of a gastric implantable device using PCA, CCA, EFICA, EMD, Wavelet, CNN, and the proposed method.

[21] N. Tremblay, P. Borgnat, Graph wavelets for multiscale community mining, IEEE Transactions on Signal Processing 62 (2014) 5227–5239.

[22] D. Boscaini, J. Masci, E. Rodolà, M. Bronstein, Learning shape correspondence with anisotropic convolutional neural networks, Advances in neural information processing systems 29 (2016).

[23] J. H. Giraldo, T. Bouwmans, Graphbgs: Background subtraction via recovery of graph signals, in: 2020 25th International Conference on Pattern Recognition (ICPR), IEEE, 2021, pp. 6881–6888.

[24] J. Wu, F. Wu, Q. Yang, Y. Zhang, X. Liu, Y. Kong, L. Senhadji, H. Shu, Fractional spectral graph wavelets and their applications, Mathematical Problems in Engineering 2020 (2020) 2568179.

[25] I. Jolliffe, Principal component analysis, Springer Verlag, New York, 2002.

[26] W. De Clercq, A. Vergult, B. Vanrumste, W. Van Paesschen, S. Van Huffel, Canonical correlation analysis applied to remove muscle artifacts from the electroencephalogram, IEEE Transactions on Biomedical Engineering 53 (2006) 2583–2587.

[27] M. Yin, J. Gao, Z. Lin, Laplacian regularized low-rank representation and its applications, IEEE transactions on pattern analysis and machine intelligence 38 (2015) 504–517.

[28] E. J. Candès, X. Li, Y. Ma, J. Wright, Robust principal component analysis?, J. ACM 58 (2011).

[29] W. Sun, Q. Du, Graph-regularized fast and robust principal component analysis for hyperspectral band selection, IEEE Transactions on Geoscience and Remote Sensing 56 (2018) 3185–3195.

[30] N. Shahid, N. Perraudin, V. Kalofolias, G. Puy, P. Vandergheynst, Fast robust pca on graphs, IEEE Journal of Selected Topics in Signal Processing 10 (2015) 740–756.

[31] F. Shang, L. Jiao, F. Wang, Graph dual regularization non-negative matrix factorization for co-clustering, Pattern Recognition 45 (2012) 2237–2250. Brain Decoding.

[32] X. Han, Robust Low-Rank Tensor Approximations Using Group Sparsity, Ph.D. thesis, Université de Rennes, 2019. URL: https://theses.fr/api/v1/document/2019REN1S001.

[33] D. Safieddine, A. Kachenoura, L. Albera, G. Birot, A. Karfoul, A. Pasnicu, A. Biraben, F. Wendling, L. Senhadji, I. Merlet, Removal of muscle artifact from eeg data: comparison between stochastic (ica and cca) and deterministic (emd and wavelet-based) approaches, EURASIP Journal on Advances in Signal Processing 2012 (2012) 1–15.

[34] Z. Koldovsky, P. Tichavsky, E. Oja, Efficient variant of algorithm fastica for independent component analysis attaining the cramér-rao lower bound, IEEE Transactions on neural networks 17 (2006) 1265–1277.

[35] J. Fleureau, J.-C. Nunes, A. Kachenoura, L. Albera, L. Senhadji, Turning tangent empirical mode decomposition: a framework for mono- and multivariate signals, IEEE Transactions on signal Processing 59 (2010) 1309–1316.

[36] S. K. Ghosh, R. K. Tripathy, et al., Evaluation of performance metrics and denoising of pcg signal using wavelet based decomposition, in: 2020 IEEE 17th India council international conference (INDICON), IEEE, 2020, pp. 1–6.

[37] S. A. Alali, A. Kachenoura, L. Albera, A. I. Hernandez, C. Michel, L. Senhadji, A. Karfoul, Optimized cnn-based denoising strategy for enhancing longitudinal monitoring of heart failure, Computers in Biology and Medicine 184 (2025) 109430.

[38] A. M. Katz, Physiology of the Heart, Lippincott Williams & Wilkins, 2010.

[39] S. Li, F. Li, S. Tang, W. Xiong, et al., A review of computer-aided heart sound detection techniques, BioMed research international 2020 (2020).

[40] D. Kong, J. Liu, B. Liu, X. Bao, Uncorrelated group lasso, Proceedings of the AAAI Conference on Artificial Intelligence 30 (2016).

[41] Z. Ma, F. Nie, Y. Yang, J. R. R. Uijlings, N. Sebe, Web image annotation via subspace-sparsity collaborated feature selection, IEEE Transactions on Multimedia 14 (2012) 1021–1030.

[42] A. Saltelli, S. Tarantola, F. Campolongo, M. Ratto, et al., Sensitivity analysis in practice: a guide to assessing scientific models, volume 1, Wiley Online Library, 2004.

[43] R. C. Alvarez, Subcutaneous monitoring of cardiac activity for chronically implanted medical devices, Ph.D. thesis, Université Paris-Saclay, 2020. URL: https://theses.hal.science/tel-03124735.